catalysts

MDPI

Article

Mechanistic Insights into the Formation of Hydrogen Cyanide on Cu-SSZ-13 Zeolites During Ammonia-Assisted Selective Catalytic Reduction in the Presence of Formaldehyde: A Perspective from Ab Initio Energetic Span Modelling

Shengming Tang [1], Ning Lu [1], Peirong Chen [2,3] and Abhishek Khetan [1,*]

[1] Junior Professorship of Multi-Scale Modeling of Heterogenous Catalysis in Energy Systems, The Integrated Fuel & Chemical Science Center, Rheinisch-Westfälische Technische Hochschule Aachen, Schinkelstraße 8, 52062 Aachen, Germany; stang@modes.rwth-aachen.de (S.T.)
[2] National Engineering Laboratory for VOCs Pollution Control Technology and Equipment, Guangzhou 510006, China
[3] Guangdong Provincial Key Laboratory of Atmospheric Environment and Pollution Control, School of Environment and Energy, South China University of Technology, Guangzhou 510006, China
* Correspondence: askhetan@modes.rwth-aachen.de

Abstract

The emission of hydrogen cyanide (HCN) from formaldehyde (CH_2O) during ammonia-assisted selective catalytic reduction (NH_3-SCR) remains a critical challenge for aftertreatment of bio-hybrid fuel combustion exhaust. The mechanistic details of HCN formation are still poorly understood, especially on widely deployed commercial catalysts like Cu-SSZ-13. In this work, we employed density functional theory calculations in combination with the Energetic Span Model to elucidate HCN formation pathways from CH_2O in the presence of NO_2 and H_2O over Cu-SSZ-13. The results revealed the HCN formation pathway with intermediate methylene imine as the dominant one under typical reaction conditions. These findings resonate very well with reports of hexamethylenetetramine (HMT) formation during NH_3-SCR with CH_2O, for which methylene imine is a critical intermediate. Turnover frequency (TOF) estimations highlighted the strong influence of NO_2 and H_2O: higher NO_2 concentrations promoted CO selectivity and suppressed HCN by oxidizing CH_2O to HCOOH, while lower H_2O enhanced HCN formation. These findings establish a detailed mechanistic framework for HCN emission on Cu-SSZ-13 and suggest that controlling NO_2/NO_x ratios and water content can mitigate HCN formation during NH_3-SCR.

Keywords: HCN emission; HCN abatement; energetic span model; NH_3-SCR; exhaust gas aftertreatment

Check for updates

Academic Editor: Changjin Tang

Received: 31 March 2026
Revised: 1 May 2026
Accepted: 17 May 2026
Published: 21 May 2026

Copyright: © 2026 by the authors. Licensee MDPI, Basel, Switzerland. This article is an open access article distributed under the terms and conditions of the Creative Commons Attribution (CC BY) license.

1. Introduction

Bio-hybrid fuels derived from biomass and renewable electricity are promising candidates to replace traditional fossil-based fuels in combustion processes for cleaner and more sustainable power generation. However, their combustion leads to the emission of many harmful gases, including nitrogen oxides (NO_x), CO, and soot, all of which require aftertreatment [1]. A standard technology to reduce NO_x emissions is selective catalytic reduction (SCR) [2]. Commercially, SCR using NH_3 as reducing agent has been implemented with catalyst materials ranging from Cu-exchanged zeolites [3] to titania-supported vanadium-tungsten oxides [4]. The overall NH_3-SCR mechanism includes the Standard-SCR, Fast-SCR,

and NO_2-SCR pathways, wherein the NO_2/NO_x ratio is a key factor determining the dominant pathway [3,4]. Over the last decade, the detailed mechanism of NH_3-SCR has been extensively investigated for both zeolite- and vanadium-based catalysts [5–8]. The ideal case involves an equimolar amount of NO and NO_2 for Fast-SCR, whereas Standard-SCR follows a similar reaction mechanism to Fast-SCR, with an additional NO oxidation step [5,8,9].

In addition to soot, CO, and NO_x, the combustion of bio-hybrid fuels also produces other species in significant amounts, such as formaldehyde (CH_2O) [1,10–12]. Multiple studies investigating the effect of CH_2O in the exhaust gas stream during NH_3-SCR have reported the formation of hydrogen cyanide (HCN), a well-known hazardous chemical [13–18]. Several mechanistic pathways for HCN formation have been proposed, along with various factors that influence this process [1].

Zengel et al. [14] performed NH_3-SCR experiments on various catalysts for NO_x removal in the presence of CH_2O under standard SCR conditions. They reported higher HCN emissions at 500 °C compared to 250 °C over V_2O_5/WO_3-TiO_2 (VWTi), Fe-ZSM-5, and Fe-BEA, whereas the opposite trend was observed over Cu-SSZ-13 [14]. Elsener and Nuguid et al. [13,17] conducted similar experiments over VWTi to investigate the effect of water on HCN emissions and found that increasing the water concentration decreases the selectivity of CH_2O conversion toward HCN while increasing selectivity toward CO_x. They also reported that when formic acid (HCOOH) was used instead of CH_2O, HCN formation occurred only in the absence of water. Ngo et al. [18] reported small amounts of adsorbed hexamethylenetetramine (HMT, $(CH_2)_6N_4$) below 250 °C. They further performed experiments over VWTi by bypassing CH_2O and instead using formamide ($HCONH_2$) and still observed HCN formation. These results suggest the role of $HCONH_2$ as a key intermediate.

Unlike VWTi, the formation of HCN on Cu-SSZ-13 catalysts is less explored and less well understood [14,15,19]. NH_3-SCR experiments with CH_2O on Cu-SSZ-13 conducted by Schönberger et al. [15] reported that HCN emissions can be tuned by the NO_2/NO_x ratio in the temperature range of 200–250 °C. They also observed the presence of adsorbed HMT and smaller amounts of $HCONH_2$. They suggested that HMT is a key intermediate for HCN formation, and that the introduction of NO_2 can intercept these intermediates, thereby decreasing HCN formation. While HCN formation had previously been reported to occur only at lower temperatures [14,15], Barth et al. [19] recently demonstrated that HCN emissions in NH_3-SCR with CH_2O can also occur at relatively higher temperatures (>350 °C), depending on the Si/Al ratio and Cu loading. Based on current evidence, HCN formation occurs differently over VWTi and Cu-SSZ-13 in terms of temperature dependence and key intermediates. Thus, the mechanistic understanding of HCN formation on VWTi does not directly apply to Cu-SSZ-13 catalysts. In addition, an increase in the NO_2/NO_x ratio has been shown to reduce HCN emissions [15], which could provide an opportunity to tune engine-out conditions for low NO_x as well as HCN emissions.

While some adsorbed species ($HCONH_2$ and HMT) common to VWTi have also been detected on Cu-SSZ-13 [15], their relevance as either spectator species or rate-determining intermediates remains unclear. Therefore, it is important to elucidate the HCN formation mechanism on Cu-SSZ-13 catalysts and to investigate the role of the NO_2/NO_x ratio. Elsener et al. [13] proposed three pathways for HCN formation over VWTi, as well as its decomposition to CO (Figure 1). These pathways provide a useful starting point for further investigations to determine their relative contributions over Cu-SSZ-13.

In this work, we performed quantum chemical simulations using a cluster model of the Cu-SSZ-13 catalyst to investigate various HCN formation pathways during NH_3-SCR in the presence of CH_2O. A primary objective of this study is to determine whether Cu sites catalyze HCN formation compared to a simple gas-phase reaction. Another objective is to understand the role of NO_2, which we assume, without any loss of generality, to be

the primary oxidant in the intermediate steps. The free energies and activation barriers for the various pathways were calculated and subsequently employed to estimate overall turnover frequencies (TOFs) using the Energetic Span Model [20,21]. Comparison of these TOFs provides detailed insights into the factors affecting HCN formation, such as NO_2 concentration, H_2O concentration, and the oxidation state and coordination of the Cu sites. Our results elucidate the important role of H_2O in HCN formation and partially capture the effect of high NO_2 content in decreasing HCN emissions.

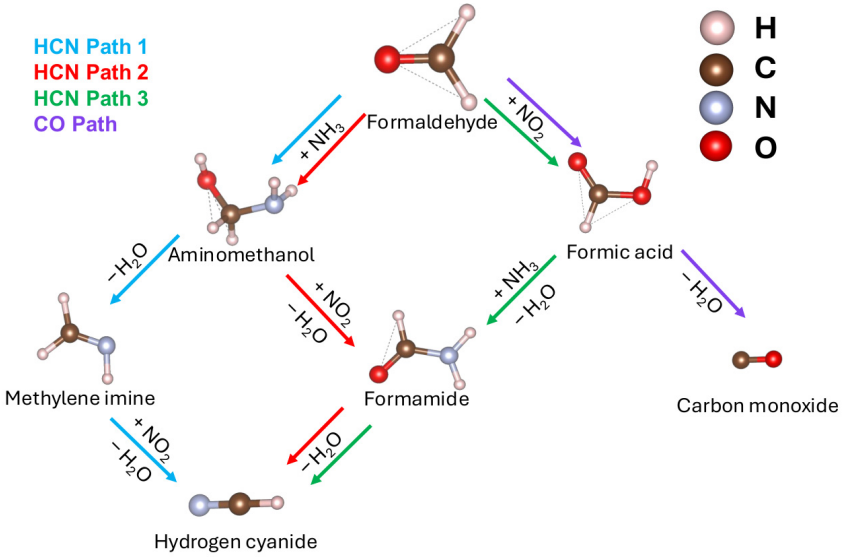


Figure 1. Reaction pathways for HCN and CO formation from formaldehyde, with NO_2 as the oxidizing agent [13].

2. Results

Figure 2 shows the free energy diagram of HCN pathway P-1 (CH_2O > NH_2CH_2OH > CH_2NH > HCN), which is described schematically in Figure 1 and in mechanistic detail in the Supporting Information (SI). Figure 2a presents the reactions in the gas phase, while Figure 2b (2c) shows the corresponding catalyzed reactions on Z_2-1 (Z-1) sites, starting from NH_3 adsorption and ending with HCN desorption. Z_2-1 represents the Cu^{2+} site with two Al atoms and one adsorbed NH_3, Z_2-2 represents the Cu^{2+} site with two Al atoms and two adsorbed NH_3, whereas Z-1 represents the Cu^{+} site with one Al atom and one adsorbed NH_3. Without loss of generality, the oxidation steps in all pathways are assumed to proceed via NO_2. In the mechanism proposed here, the oxidation of CH_2NH to HCN involves an initial H abstraction leading to the formation of HONO, followed by a second H abstraction resulting in the release of H_2O and NO. It should be noted that there is substantial experimental evidence supporting HONO as an intermediate species in NH_3-SCR [6,22].

Comparing our results with the 0 K energies reported in the literature [23] (in parentheses), the enthalpic reaction barriers in the gas phase are TS1 [CH_2O > NH_2CH_2OH] = 1.34 (1.43) eV, and TS2 [NH_2CH_2OH > CH_2NH] = 2.33 (2.43) eV. The small differences of ~0.1 eV likely arise from the use of the M06-2X functional with the 6-311++G(3df,3pd) basis set for geometry optimization, followed by single-point energy calculations at the CCSD(T)/6-311++G(3df,3pd) level in the literature [23]. Despite employing a relatively less computationally demanding exchange-correlation functional in this work, similar values are obtained.

As shown in Figure 2a for the gas phase reaction, I_1 [NH_3 + CH_2O] is the TDI and T_2 [NH_2CH_2OH*] is the TDTS. For the catalyzed reaction on Z_2-1, however, I_2 [*NH_3 + CH_2O] is the TDI and T_4 [*CH_2N. . .HONO] is the TDTS (Figure 2b). Similarly, on Z-1, I_2 [*NH_3 +

CH_2O] is the TDI and T_4 [*CH_2N. . .HONO] is the TDTS (Figure 2c). It can be seen that the energy span (i.e., G_{TDTS}-G_{TDI}) is 2.51 eV for the gas-phase reaction, compared to 2.28 eV on Z_2-1 and 1.93 eV on Z-1 for the catalyzed reactions. Clearly, catalysis affects not only the reaction barriers and energy spans but also the identities of the TDIs and TDTSs. In the gas phase, the dehydration of [NH_2CH_2OH*] limits the TOF of the overall reaction, whereas for the catalyzed reaction on Z_2-1 and Z-1, NH_2CH_2OH dehydration is comparably faster, and CH_2NH oxidation becomes the TOF-determining transition state. This provides the first theoretical indication that HCN formation via pathway P-1 can indeed be catalyzed on both Z_2-1 and Z-1 sites.

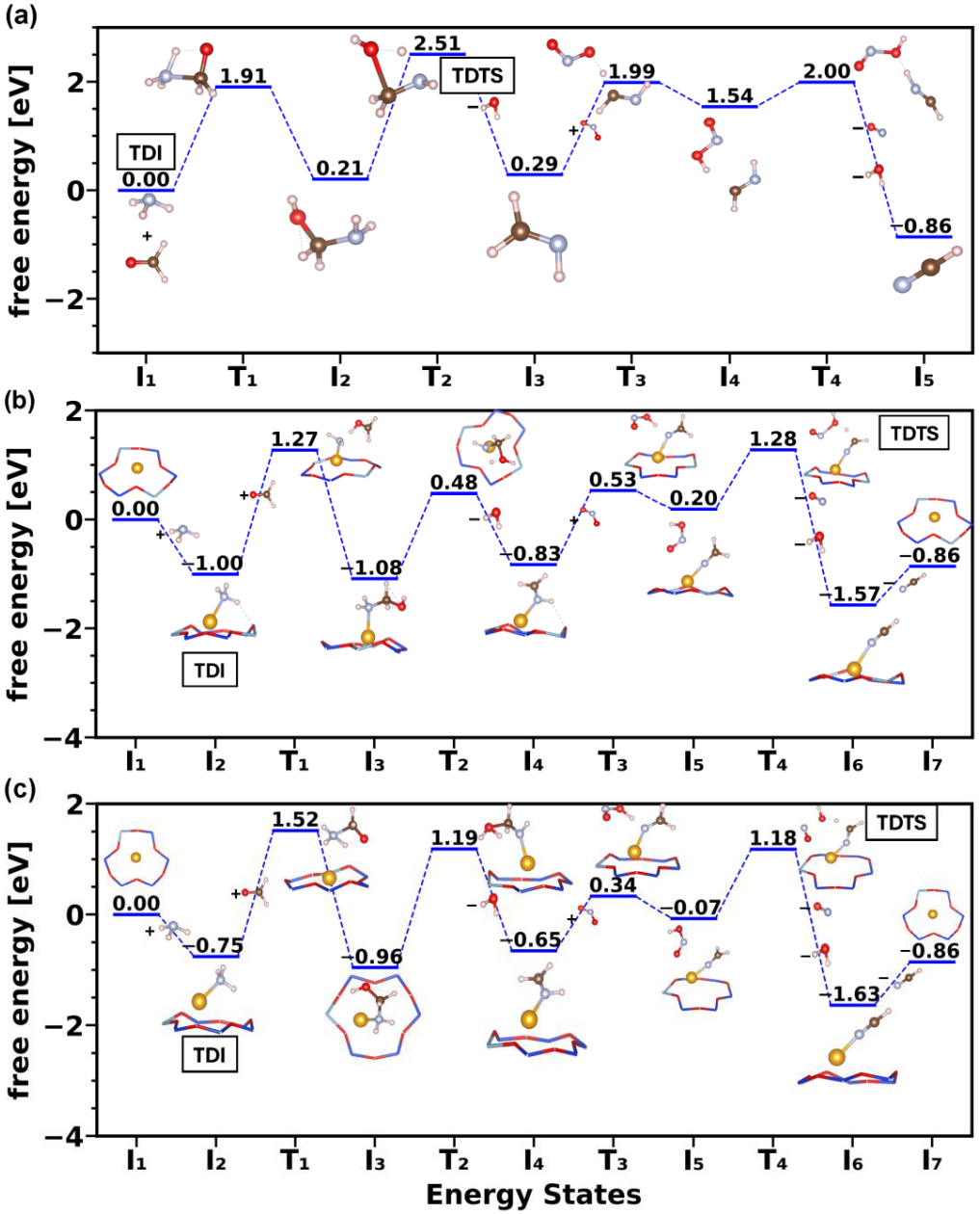


Figure 2. Free energy diagram (at 473 K) for HCN formation via pathway P-1 CH_2O > NH_2CH_2OH > CH_2NH > HCN, (**a**) in the gas phase, (**b**) on Z_2-1 sites, (**c**) on Z-1 sites. Atom colors: Cu, yellow; H, white; O, red; C, brown; N, gray.

Next, to estimate the reaction rate in terms of the TOF, the effect of the species concentrations was considered. Within the energetic span approximation, only the concentrations of species that enter or exit the reaction cycle between the TDI and TDTS need to be taken

into account. For the gas-phase reaction, NH_3 and CH_2O enter the reaction cycle, while no species exit the cycle. In contrast, for the catalyzed reaction on Z_2-1, Z_2-2, and Z-1, CH_2O and NO_2 enter the reaction cycle, while H_2O exits between the TDI and TDTS.

The TOFs for this HCN formation pathway, accounting for species concentrations in the gas phase and on the Z_2-1 and Z-1 sites, can be expressed by Equations (1) and (2), respectively.

$$\mathrm{TOF}_{\mathrm{g}}^{1} = \frac{k_B T}{h} e^{-\frac{\Delta G}{k_B T}} \prod [NH_3][CH_2O] \quad (1)$$

$$\mathrm{TOF}_{Z2}^{1} = \mathrm{TOF}_{\mathrm{Z}}^{1} = \frac{k_B T}{h} e^{-\frac{\Delta G}{k_B T}} \prod \frac{[CH_2O][NO_2]}{[H_2O]} \quad (2)$$

TOF estimation is highly sensitive to the calculated free energies and activation barriers due to the exponential dependence. The B3LYP/DEF2-SVP level of theory was employed in this study to achieve convergence in barrier calculations within a reasonable computational time. However, this approach is prone to systematic errors, as shown by comparison with the more accurate DLPNO-CCSD(T) level of theory in Figure S1. Consequently, our calculations may overestimate the binding energies (i.e., more negative adsorption energies) of molecules on Cu sites and may therefore systematically underestimate the TOFs. For this reason, we report relative TOF values, taking the lowest TOF as the reference (Table 1). The estimated relative TOFs of the reaction cycles increase from 2.95×10^6 in the gas phase to 8.52×10^8 on the Z_2-1 and 3.56×10^{12} on the Z-1 catalyst model. These relative TOFs further confirm that the reaction is catalyzed. It is also evident that the oxidation state of Cu has a significant effect, with Cu in the +1 state (Z-1) catalyzing the reaction approximately 10^3 times faster than in the +2 state.

Table 1. TDI, TDTS, energy span, important species and relative TOF results of different pathways and active sites.

Path (Active Site)	TDI [Species]	TDTS [Species]	[*Species Entering*] / [*Species Exiting*]	Ener. Span (eV)	Rel. TOF
P-CO (Gas)	$I_1[CH_2O + NO_2]$	$T_1[CH_2O...NO_2]$	$[CH_2O][NO_2]$	2.44	3.87×10^4
P-CO (Z_2-1)	$I_4[*HCOOH + H_2O]$	$T_1[*CH_2O...NO_2]$	$\frac{[CH_2O][NO_2]}{[H_2O][CO]}$	1.97	1.39×10^{18}
P-CO (Z_2-2)	$I_5[*HCOOH + H_2O]$	$T_1[*CH_2O...NO_2]$	$\frac{[CH_2O][NO_2]}{[H_2O]^2[CO]}$	2.53	5.31×10^{14}
P-CO (Z-1)	$I_5[*HCOOH + H_2O]$	$T_3[*HCOOH...H_2O]$	$[H_2O]$	2.33	6.77×10^{17}
P-1 (Gas)	$I_1[NH_3 + CH_2O]$	$T_2[NH_2CH_2OH*]$	$[CH_2O][NO_2]$	2.51	2.95×10^6
P-1 (Z_2-1)	$I_2[*NH_3 + CH_2O]$	$T_4[*CH_2N...HONO]$	$\frac{[CH_2O][NO_2]}{[H_2O]}$	2.28	8.52×10^8
P-1 (Z_2-2)	$I_2[*NH_3 + CH_2O]$	$T_3[*CH_2NH...NO_2]$	$\frac{[CH_2O][NO_2]}{[H_2O]}$	2.20	3.80×10^9
P-1 (Z-1)	$I_2[*NH_3 + CH_2O]$	$T_4[*CH_2N...HONO]$	$\frac{[CH_2O][NO_2]}{[H_2O]}$	1.93	3.56×10^{12}
P-2 (Gas)	$I_4[HCONH_2 + H_2O]$	T_2 $[NH_2CH_2OH...NO_2]$	$\frac{[NH_3][CH_2O][NO_2]}{[H_2O][HCN]}$	2.58	9.98×10^6
P-2 (Z_2-1)	$I_5[*HCONH_2 + H_2O]$	T_3 $[*NH_2CH_2OH...NO_2]$	$\frac{[NH_3][CH_2O][NO_2]}{[H_2O][HCN]}$	3.11	2.40×10^1
P-2 (Z_2-2)	$I_5[*HCONH_2 + H_2O]$	T_3 $[*NH_2CH_2OH...NO_2]$	$\frac{[NH_3][CH_2O][NO_2]}{[H_2O][HCN]}$	3.20	2.18

Table 1. *Cont.*

Path (Active Site)	TDI [Species]	TDTS [Species]	$\frac{[Species\ Entering]}{[Species\ Exiting]}$	Ener. Span (eV)	Rel. TOF
P-2 (Z-1)	I_7[*$HCONH_2$ + H_2O]	T_3 [*NH_2CH_2OH...NO_2]	$\frac{[NH_3][CH_2O][NO_2]}{[H_2O][HCN]}$	3.05	6.92×10^1
P-3 (Gas)	I_2 [HCOOH + NH_3 + H_2O]	T_1[CH_2O...NO_2]	$\frac{[NH_3][CH_2O][NO_2]}{[H_2O]^2[HCN]}$	3.48	1
P-3 (Z_2-1)	I_5 [*HCOOH + *NH_3 + H_2O]	T_1[*CH_2O...NO_2]	$\frac{[CH_2O][NO_2]}{[H_2O]^2[HCN]}$	3.60	3.47×10^3
P-3 (Z_2-2)	I_8 [*$HCONH_2$ + H_2O]	T_1[*CH_2O...NO_2]	$\frac{[CH_2O][NO_2]}{[H_2O]^3[HCN]}$	3.89	1.19×10^3
P-3 (Z-1)	I_6 [*HCOOH + *NH_3 + H_2O]	T_1[*CH_2O...NO_2]	$\frac{[CH_2O][NO_2]}{[H_2O]^2[HCN]}$	3.19	6.62×10^7

XXX represents adsorbed species. XXX represents activated species.

Following the same methodology as described above, we performed calculations for all other pathways and catalyst models. Pathways P-2 and P-3 both involve the key intermediate $HCONH_2$, which has been reported in several NH_3-SCR studies on HCN formation [13–15,17,18]. In line with previous computational studies [24,25], we modeled the decomposition of formamide ($HCONH_2$) via an additional intermediate step involving NHCHOH ($HCONH_2$ > NHCHOH > HCN), with H_2O acting as a catalyst. The detailed mechanisms are provided in the SI.

Comparing our results with literature [24,25], the enthalpic reaction barrier for $HCONH_2$ decomposition to HCN in the gas phase, with one H_2O molecule acting as a catalyst, is 2.44 (2.42 [25], 2.46 [24]) eV. These literature results were obtained using B3LYP/6-31++G(d,p) calculations [25] and MP2/aug-cc-pVTZ optimizations followed by CCSD(T)/CBS single-point calculations [24]. Despite the use of different levels of theory, our results show good agreement with the reported values. For the same reaction over catalysts, no direct literature values were found. However, the free energy barrier reported over silica is 2.13–2.27 eV [26], which is comparable to our value of 2.27 eV on the Z_2-1 catalyst. Finally, our calculated gas-phase reaction barrier for the HCOOH decomposition process catalyzed by H_2O is 1.94 eV, which differs from literature values of 2.09 [27] and 2.14 [28] eV. This discrepancy likely arises from the use of the def2-SVP basis set in our calculations, as opposed to the 6-311G(d,p) basis set used in the referenced studies.

The free energy diagrams of HCN formation via pathways P-2 (CH_2O > NH_2CH_2OH > $HCONH_2$ > HCN) and P-3 (CH_2O > HCOOH > $HCONH_2$ > HCN) are shown in Figures 3 and 4, respectively. The TDIs, TDTSs, energy spans and relative TOFs of all three pathways in the gas phase and over the two catalyst models are summarized in Table 1. As shown in Table 1, even for the same reaction pathway, different catalyst models exhibit different TDI and TDTS, and consequently, different relative TOFs.

Figure 3 (Table 1) shows that HCN formation along P-2 has an energy span of 2.58 eV, which increases to 3.11 eV and 3.05 eV on the Z_2-1 and Z-1 sites, respectively. Correspondingly, the relative TOF in the gas phase along P-2 is 9.98×10^6, which decreases to 2.40×10^1 and 6.92×10^1 on the Z_2-1 and Z-1 sites, respectively. These estimates indicate that the gas-phase P-2 pathway is preferred over the catalyzed P-2 pathway.

Figure 4 (Table 1) shows that the energy span of 3.48 eV for P-3 in the gas phase changes to 3.60 eV and 3.19 eV on the Z_2-1 and Z-1 sites, respectively. The relative TOF of 1 in the gas phase increases to 3.47×10^3 and 6.62×10^7 on Z_2-1 and Z-1, respectively. Notably, although the energy span for Z_2-1 is not lower than that of the gas phase, the relative TOF on Z_2-1 is significantly higher. These estimates highlight the importance of

including concentration effects in relative TOF calculations. Furthermore, both Z_2-1 and Z-1 exhibit higher relative TOFs along P-3 compared to the gas phase.

The results in Table 1 show that, irrespective of the catalyst model, the relative TOFs for the catalyzed pathways follow the trend P-1 > P-3 > P-2. From a mechanistic perspective, the lower relative TOFs for P-2 and P-3 can be attributed to the high relative stability of the TDIs, namely $HCONH_2$ (P-2) and HCOOH (P-3). For P-2, on the Z_2-1 (Z-1) site, adsorbed $HCONH_2$ exhibits a significantly lower free energy of −3.03 eV (−3.11 eV) relative to the initial state, as shown in Figure 3b (3c). Similarly, for P-3, on the Z_2-1 (Z-1) site, HCOOH has a low free energy of −3.43 eV (−3.01 eV) relative to the initial state, as shown in Figure 4b (4c). These calculations help explain, at least in part, why formamide and formic acid are routinely detected in experiments using diffuse reflectance infrared Fourier transform (DRIFT) spectroscopy [14,15,17].

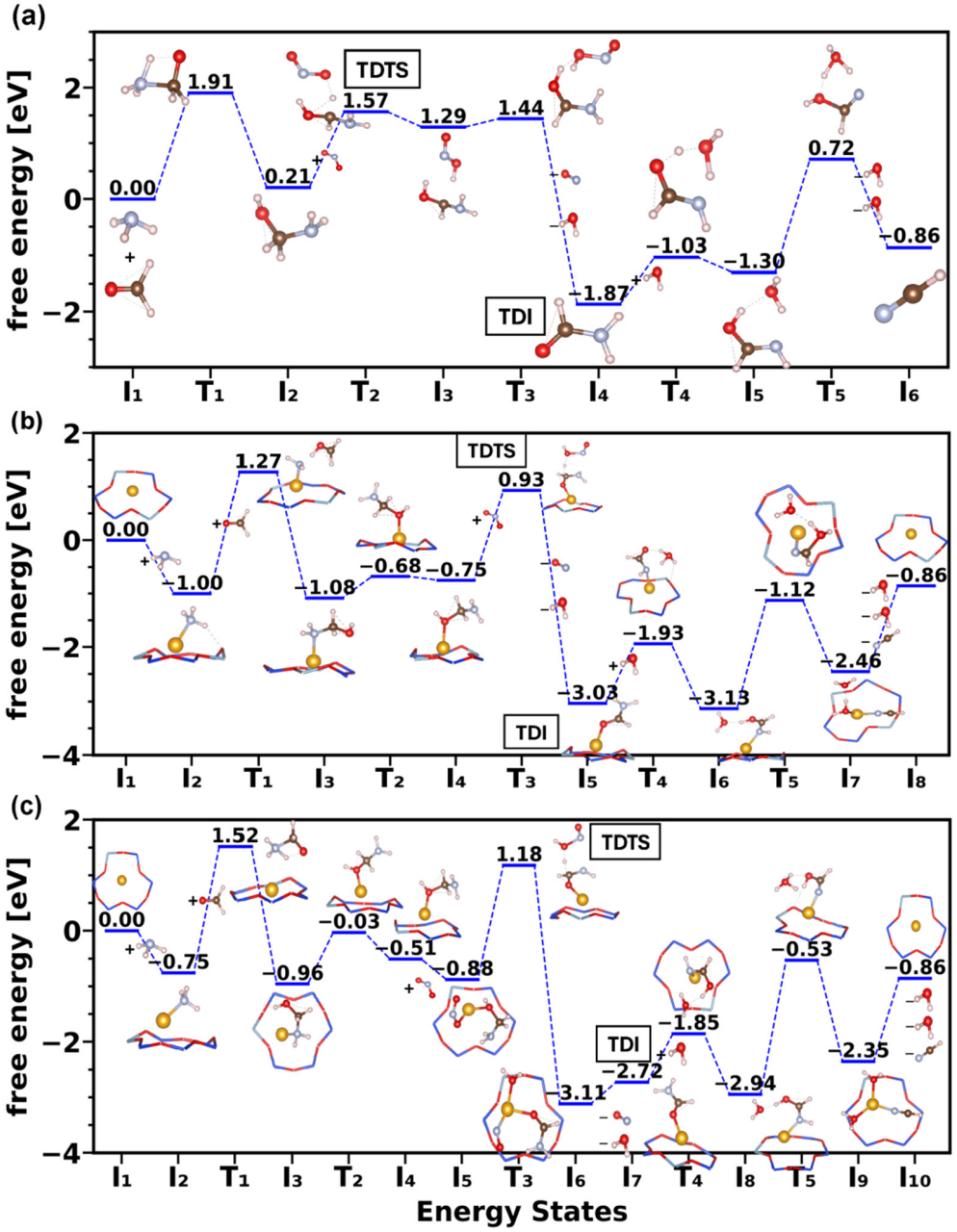


Figure 3. Free energy diagram (at 473 K) for HCN formation via pathway P-2 CH_2O > NH_2CH_2OH > $HCONH_2$ > HCN, (**a**) in the gas phase, (**b**) on Z_2-1 sites, and (**c**) on Z-1 sites. Atom colors: Cu, yellow; H, white; O, red; C, brown; N, gray.

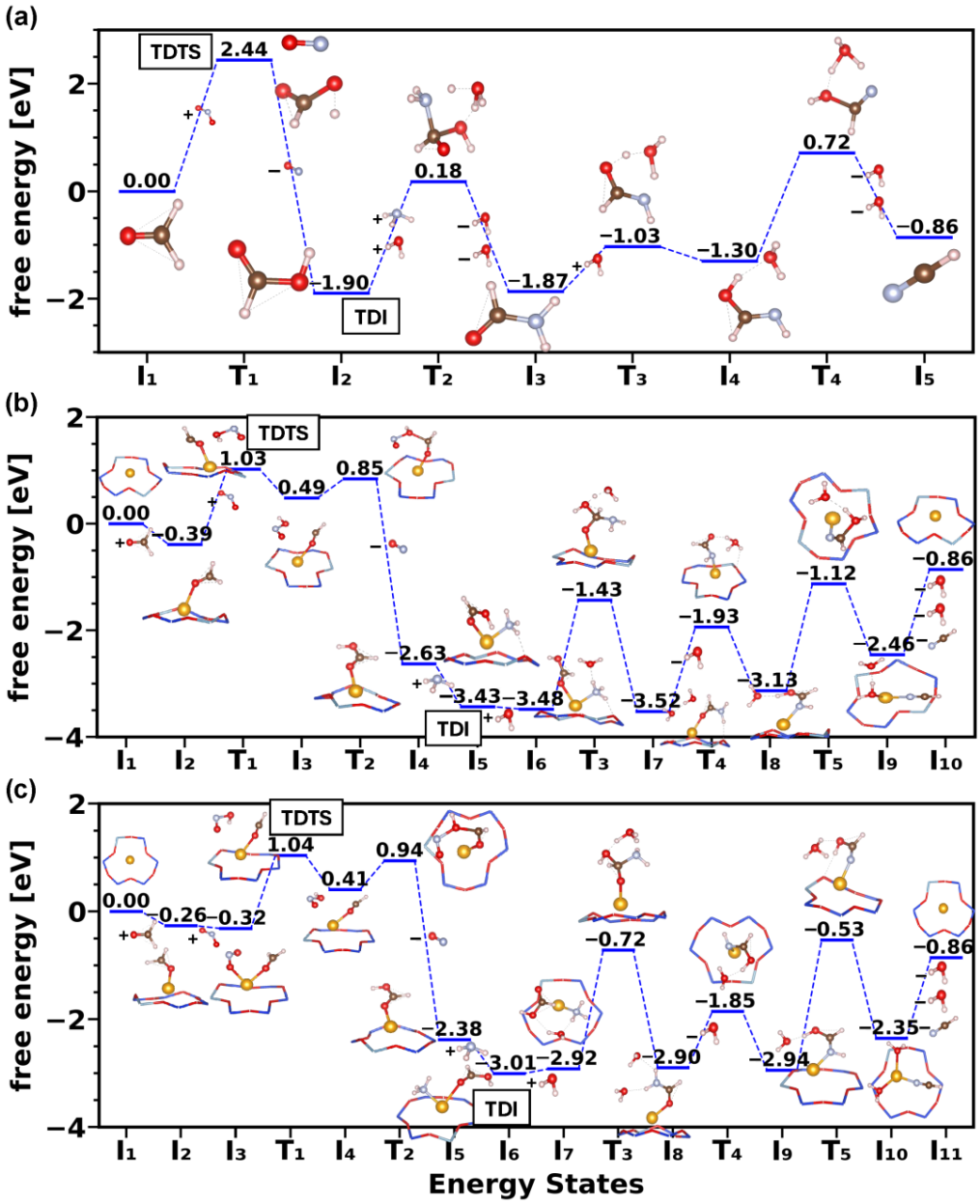


Figure 4. Free energy diagram (at 473 K) for HCN formation via pathway P-3 CH_2O > HCOOH > $HCONH_2$ > HCN, (**a**) in the gas phase, (**b**) on Z_2-1 sites, and (**c**) on Z-1 sites. Atom colors: Cu, yellow; H, white; O, red; C, brown; N, gray.

Next, we consider P-CO, a competing pathway to HCN formation starting from CH_2O (CH_2O > HCOOH > CO). The P-CO involves formaldehyde oxidation to formic acid, followed by formic acid decomposition to CO and H_2O. The detailed mechanism is provided in the SI. In this work, all formic acid decomposition reactions were modeled with H_2O acting as a catalyst. In the gas phase at 0 K, formic acid decomposition without H_2O as a catalyst has an energy barrier of 3.03 eV, whereas in the presence of H_2O, the barrier decreases to 2.15 eV (Figure 5a). Experimental studies report that although formic acid is abundant during NH_3-SCR with CH_2O, HCN formation from formic acid occurs only in the absence of water [13,17]. This observation can be rationalized by the fact that formic acid decomposition to CO is significantly more favorable in the presence of water, as demonstrated by our calculations. The effect of water concentration is revisited in the following sections.

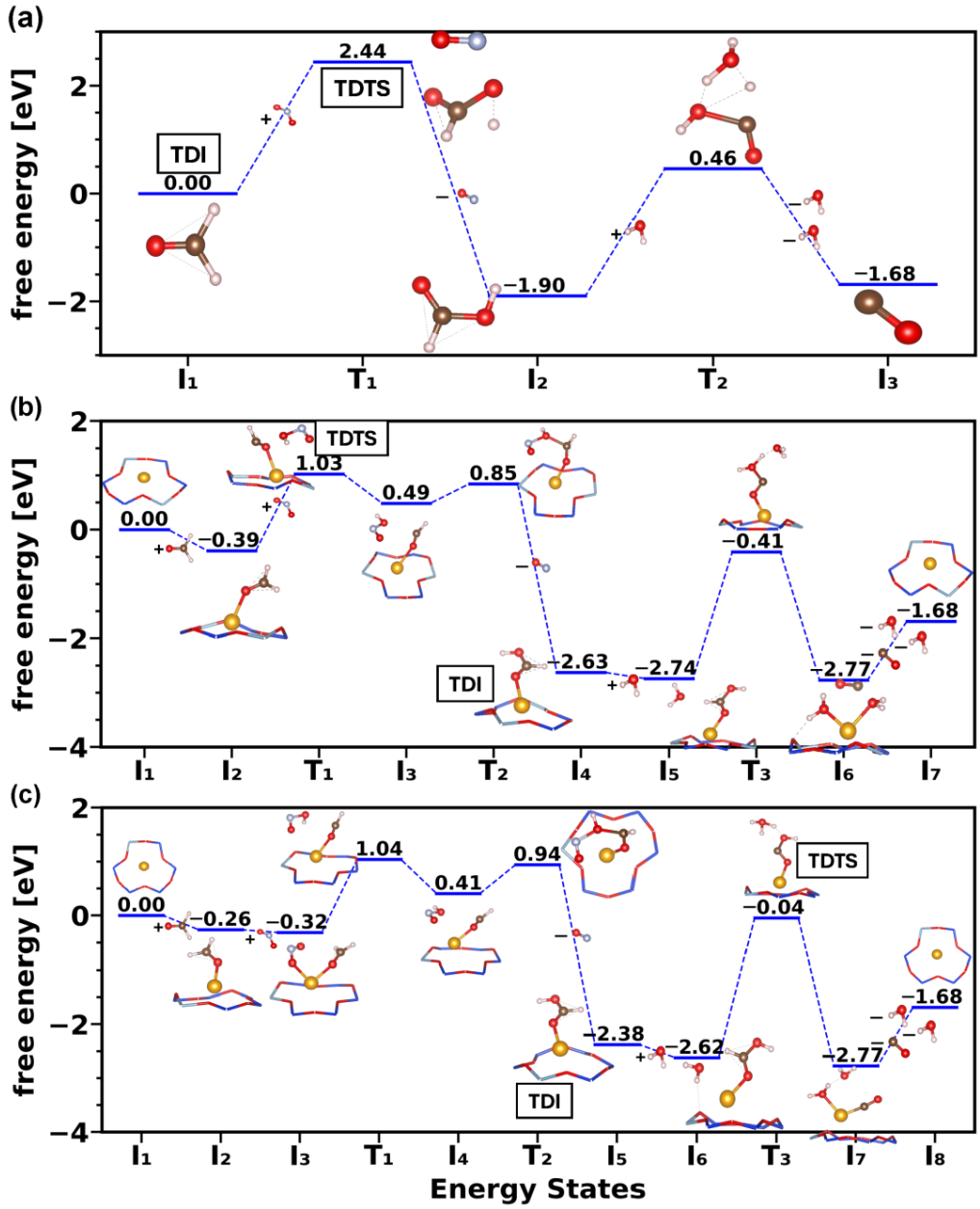


Figure 5. Free energy diagram (at 473 K) for the CO formation pathway CH_2O > HCOOH > CO, (**a**) in the gas phase, (**b**) on Z_2-1 sites, (**c**) on Z-1 sites. Atom colors: Cu, yellow; H, white; O, red; C, brown; N, gray.

The free energy diagrams of P-CO are shown in Figure 5. For this pathway, the TDI and TDTS are I_1 [CH_2O + NO_2] and T_1 [CH_2O. . .NO_2] in the gas phase; I_4[*HCOOH + H_2O] and T_1[*CH_2O. . .NO_2] on Z_2-1, and I_5[*HCOOH + H_2O] and T_3[*HCOOH. . .H_2O] on Z-1. As shown in Figure 5a, the gas-phase reaction has an energy span of 2.44 eV, whereas over the Z_2-1 and Z-1 sites (Figure 5b,c), the energy spans decrease to 1.97 eV and 2.33 eV, respectively. Accordingly, the relative TOFs increase from 3.87×10^4 in the gas phase to 1.39×10^{18} and 6.77×10^{17} on the Z_2-1 and Z-1 sites, respectively. From a mechanistic perspective, the CH_2O oxidation barrier of 2.44eV in the gas phase is significantly reduced to 1.42eV (Z_2-1) and 1.36 eV (Z-1) on the catalysts, enabling a much faster reaction.

Lastly, the Z_2-2 catalyst model shows results similar to those of the Z_2-1 model, as the relative TOFs for all three HCN pathways are within one order of magnitude, as shown in Table 1. The free energy diagrams for the Z_2-2 catalyst model are provided in Figures S2–S5 in the SI. Compared to the Z_2-1 model, however, the relative TOF of the CO pathway on the

Z_2-2 model decreases from 1.39×10^{18} to 5.31×10^{14}. This indicates that the presence of an additional co-adsorbed NH_3 molecule on Cu^{2+} sites has a limited effect on HCN formation pathways but significantly slows down CO formation.

We also considered the dynamically solvated and mobile $Cu(NH3)_2$ moiety as an active site for HCN formation and compared it with the equivalent tethered Z_2-2 model. It was found that the binding energies of all intermediates on the $Cu(NH3)_2$ moiety (Table S1) are more negative than those on the Z_2-2 model. Under the assumption that the transition states remain unchanged, the relative TOFs for the mobile $Cu(NH3)_2$ and Z_2-2 models are compared in Table S2. As can be clearly observed, irrespective of the pathway, the reaction rates are several orders of magnitude lower on the solvated and mobile $Cu(NH_3)_2$ moiety. This behavior is consistent with Sabatier's principle.

3. Discussion

A comparative summary of the relative TOFs for all pathways is shown in the bar plot in Figure 6. As expected, TOF estimation is highly sensitive to the calculated free energies and activation barriers due to the exponential dependence. Nevertheless, based on reasonable assumptions regarding the uncertainty in energy calculations, several clear conclusions can still be drawn from their comparison.

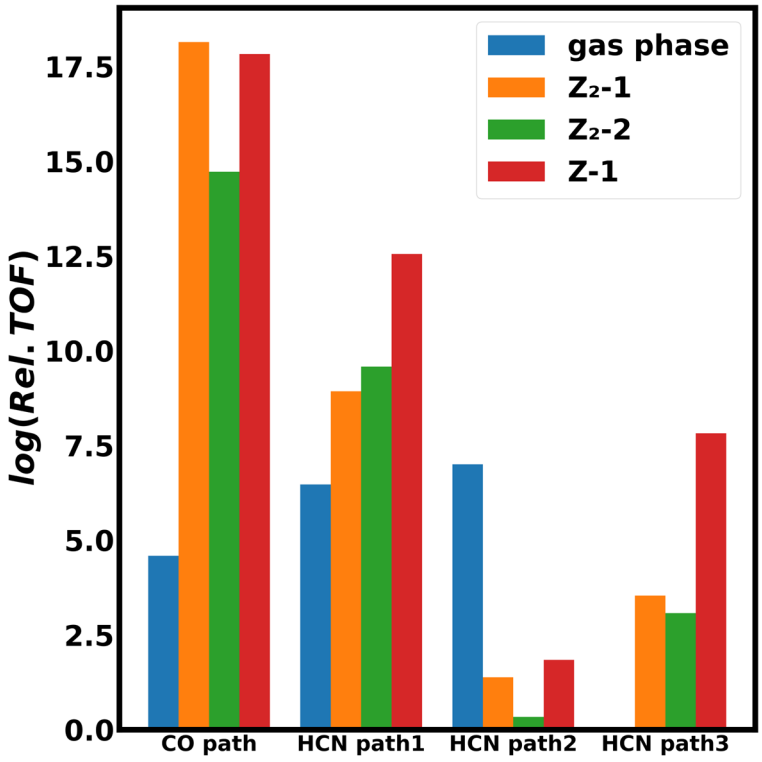


Figure 6. Relative TOFs of different pathways in the gas phase and over different active sites at a temperature of 473 K.

Assuming a typical DFT error of ~10 kcal/mol in the estimation of energies and barriers, this corresponds to a difference in relative TOFs of approximately 10^4 at 473 K, according to Equation (3). Therefore, relative TOFs that differ by ~10^4 can still be compared with a reasonable degree of confidence.

Another source of uncertainty arises from the fact that only pathways involving intermediates and reaction steps proposed in experimental studies (Figure 1) [13] were considered. If alternative pathways involving other intermediates (e.g., HMT) or more complex reaction mechanisms (e.g., on the $[(NH_3)_4Cu_2O_2]^{2+}$ complex [29]) are operative,

the relative TOFs may differ. An additional source of uncertainty is that the current analysis treats all pathways independently, whereas in reality, the reactions occur simultaneously. However, given the large differences in relative TOFs between certain pathways, even if the absolute values change with the inclusion of additional intermediates or parallel pathways, the mechanistic roles of NO_2 and H_2O, as well as their influence on product selectivity, are expected to remain valid.

First, considering only the gas-phase reactions (blue bars), pathway P-2 exhibits the highest relative TOF. It is higher than CO formation (via P-CO), although not beyond the estimated error margin (~10^4). Therefore, in the absence of a catalyst, it is difficult to conclusively determine whether HCN formation from CH_2O dominates over its decomposition to CO.

When the effect of catalysis is considered, the results indicate that HCN formation on the Z-1 site is significantly faster along pathways P-1 and P-3 compared to the gas phase. Furthermore, catalyzed CH_2O decomposition to CO is substantially faster than even the most favorable HCN formation pathways, irrespective of the catalyst model.

These observations help rationalize the experimental findings. Schoeneberger et al. [15] reported that increasing the NO_2 concentration decreases HCN emissions. Table 2 details the effect of NO_2 on HCN emissions, comparing experimental emission data [15] with calculated relative TOF values. Across the NO_2/NO_x ratio range of 0–100%, pathway P-CO consistently exhibits significantly higher relative TOFs than P-1 for HCN formation (by ~10^6). Although the relative TOF for HCN formation also increases with increasing NO_2 concentration, the simultaneous increase in CH_2O decomposition to CO occurs at much higher relative TOFs, thereby reducing the availability of CH_2O for HCN formation. This implies that HCN formation is strongly suppressed with increasing NO_2. In addition, as shown in Table 1, both gas-phase and catalyzed (on Z_2-1) P-CO pathways are directly proportional to the NO_2 concentration. These findings are in good qualitative agreement with the reported experimental data [15].

Table 2. Comparison of the experimental data [15] and calculated rel. TOF values of the NO_2 effect on CO and HCN formation during NH_3-SCR on Cu-SSZ-13 catalysts.

Exp. NO_2/NO_x Ratio (%)	Exp. [NO_2] (ppm)	Exp. [HCN] (ppm)	Calc. P-CO Rel. TOF	Calc. HCN P-1 Rel. TOF
0	1	25	1.39×10^{18}	3.56×10^{12}
50	250	23	2.19×10^{19}	6.53×10^{13}
75	375	3	2.23×10^{19}	7.16×10^{13}
100	500	2	2.25×10^{19}	7.27×10^{13}

It is important to reiterate that NO_2 is assumed to be the oxidizing agent in all pathways considered, rather than O_2 or atomic O, and it is a key intermediate in both Fast- and Standard-SCR. The presence of alternative oxidants may alter the relative TOFs, which will be addressed in future work. However, (i) O-O bond activation on mononuclear Cu sites in SSZ-13 involves additional steps with NO participation, (ii) it incurs a relatively high energy penalty at low temperatures (e.g., 1.45 eV at 0 K [30], 1.08 eV at 473 K [8], 0.89 eV at ~623 K [7]), and (iii) previous studies indicate that NO- and O_2-assisted NH_3 activation via NO_2 intermediates is more favorable than direct O_2-assisted activation on Cu-SSZ-13 [31], supporting the validity of our assumption.

Although the exact relative TOF values may change if oxidants other than NO_2 are considered, the trends, particularly the effect of H_2O concentration, are expected to remain similar. Finally, a comparative analysis of all results highlights a strong influence of the Cu oxidation state and a relatively minor effect of additional NH_3 coordination on the Z_2-1 site.

Our finding that pathway P-1 is the most dominant route for HCN formation is consistent with experimental observations of HMT formation, which has been reported during NH_3-SCR with CH_2O over Cu-SSZ-13 zeolites [15] and other catalysts [18,32]. This is because the P-1 intermediates, NH_2CH_2OH and CH_2NH, are known precursors for HMT formation at low temperatures, as demonstrated in both experiments [33] and simulations [34].

Next, we examine the important effect of H_2O on HCN formation, which has been studied in detail over VWTi catalysts [13,17]. A comparison of experimental data with our relative TOF analysis is presented in Table 3. When the H_2O concentration increases from 0 to 2.5%, the selectivity toward CO rises rapidly from 2% to 23%, as reported experimentally [13]. This trend can be correlated with a substantial increase in the relative TOF (~10^4) or in the P-CO/P-1 TOF ratio (~10^5) predicted by our calculations. These results are again in good qualitative agreement with the reported experimental data [13].

Table 3. Comparison of the experimental data [13] and rel. TOF values on the H_2O effect on CO and HCN formation during NH_3-SCR on V_2O_5/WO_3-TiO_2 catalysts.

Exp. H_2O Vol (%)	Exp. CO Sel. (%)	Exp. HCN Sel. (%)	Calc. P-CO Rel. TOF	Calc. HCN P-1 Rel. TOF	Calc. P-CO/P-1 Rel. TOF
0	2	98	3.02×10^{14}	6.97×10^{13}	4.33
2.5	23	77	3.03×10^{18}	1.03×10^{13}	2.95×10^{5}
5	30	70	2.11×10^{18}	5.53×10^{12}	3.82×10^{5}
7.5	34	66	1.48×10^{18}	3.79×10^{12}	3.91×10^{5}
10	37	63	1.11×10^{18}	2.88×10^{12}	3.86×10^{5}
12.5	40	60	8.74×10^{17}	2.32×10^{12}	3.76×10^{5}

According to our reaction models, the relative TOFs of all catalyzed pathways across all catalyst models are influenced by the H_2O concentration. Furthermore, with the exception of P-CO on Z-1, all relative TOFs are inversely proportional to [H_2O]. Notably, the relative TOFs for P-3 exhibit a stronger inverse dependence on [H_2O] than those for P-1 and P-2, as shown in Table 1.

To investigate the effect of a dry atmosphere, we considered [H_2O] = 1 ppm and re-evaluated the TDIs and TDTSs for all pathways. Within the Energetic Span Model, incorporating species concentrations can alter the identities of the TDI and TDTS. Table S3 summarizes the TDIs, TDTSs, energy spans, relevant species entering or exiting the cycle, and the resulting relative TOFs for different pathways and active sites. At 1 ppm H_2O, the TDI-TDTS combinations change for all pathways except P-2. These changes in TDIs and TDTSs lead to corresponding variations in energy spans and, consequently, in the relative TOFs.

A summary of relative TOF enhancement by water (TOF^w), comparing conditions with and without water ([H_2O] = 80,000 ppm and 1 ppm), is shown in Figure 7. The ratios of TOFs in the presence of water (80,000 ppm H_2O) to those in its absence (1 ppm H_2O) are presented in the bar plot. Positive and negative values indicate that increasing H_2O concentration increases or decreases the TOF, respectively.

The TOF^w values for HCN formation are generally negative across all pathways and catalyst models. In the gas phase, however, these values fall within the previously discussed error margin. On the catalyst models, the TOF^w for HCN formation is significantly reduced ($<10^{-4}$) across multiple pathways and catalyst configurations. In contrast, the TOF^w values for CH_2O decomposition to CO on the catalyst models are positive.

Taken together, these trends clearly indicate that increasing H_2O concentration inhibits HCN formation while promoting decomposition to CO. Similar behavior has been reported for NH_3-SCR with CH_2O over V_2O_5/WO_3-TiO_2 catalysts [13]. Notably, pathways involving

HCOOH as an intermediate (P-3 and P-CO) are strongly influenced by H_2O concentration. These findings are consistent with experimental observations over V_2O_5/WO_3-TiO_2, where HCN formation from HCOOH—an important intermediate in P-CO—occurs only in the absence of water [13,17]. Furthermore, in the absence of H_2O, pathway P-3 becomes as dominant as P-1 for HCN formation.

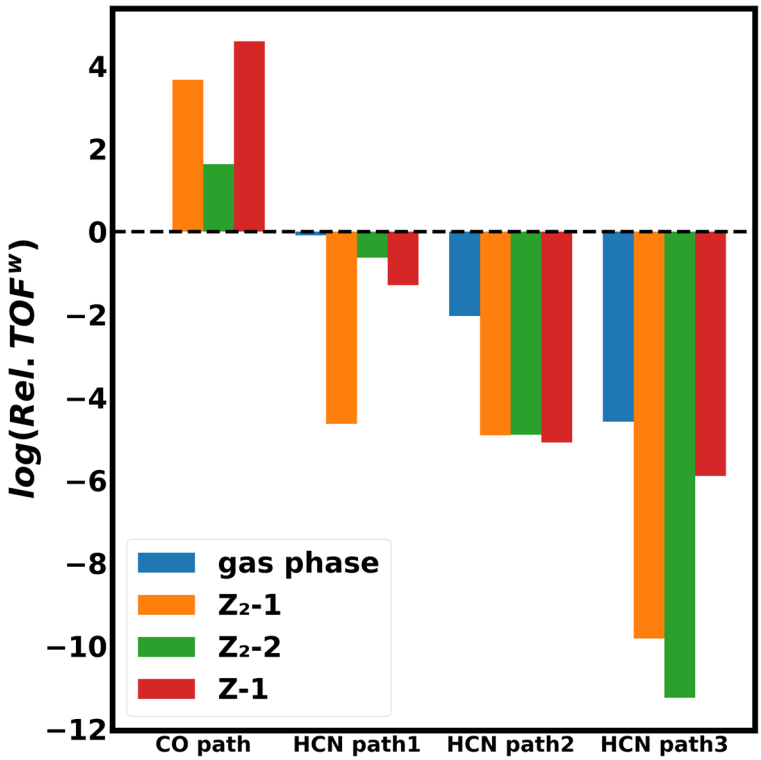


Figure 7. Relative TOF^w indicating the effect of water on different pathways at 473 K. Results are expressed as the ratio of TOF with water (80,000 ppm H_2O) to TOF without water (1 ppm H_2O). Positive and negative values indicate that increasing the H_2O concentration increases or decreases the relative TOF, respectively.

4. Methods

4.1. Catalyst Model

The Cu atom located in the six-membered (6M) ring, as shown in Figure 8a–c, where Al atoms replace the original Si atoms, represents one of the most widely used models of the active site in Cu-SSZ-13 catalysts in the literature [35]. The full periodic unit cell model of Cu-SSZ-13 (Figure 8d) contains 109 atoms (36 T sites + Cu). Reaction barrier calculations on this model are computationally demanding and difficult to converge, particularly when using the Nudged Elastic Band (NEB) method [36].

To enable the application of advanced NEB techniques, such as free-end NEB and zoom NEB, which are only implemented in specific software packages, we employed a cluster model of the catalyst (Figure 8e). Atoms were removed from the periodic structure such that only the active site 6M ring, along with all connected 4M and 8M rings, was retained. To maintain charge balance, the outermost O atoms bonded to Si were terminated with H atoms. This cluster model effectively includes at least four bonds extending from the Cu active site.

This approach is comparable to the low-error cluster model (MAE < 5 kJ/mol) reported by Goncalves et al. [37], which includes up to five bonds from the active site. The difference in the number of bonds used for cluster termination arises from the different Cu site locations considered, as their study focused on a Cu atom in a 4M ring rather than the more

stable 6M ring examined here. In this work, we considered Cu in both the Cu^{+} (Z-1) state, obtained by substituting one Si atom with Al (Figure 8c), and the Cu^{2+} (Z_2-1) state obtained by substituting two diametrically opposite Si atoms with Al (Figure 8a). To prevent spurious structural distortions, the atoms in the upper and lower "layers" were fixed to mimic their positions in the periodic lattice, as shown in Figure 8f.

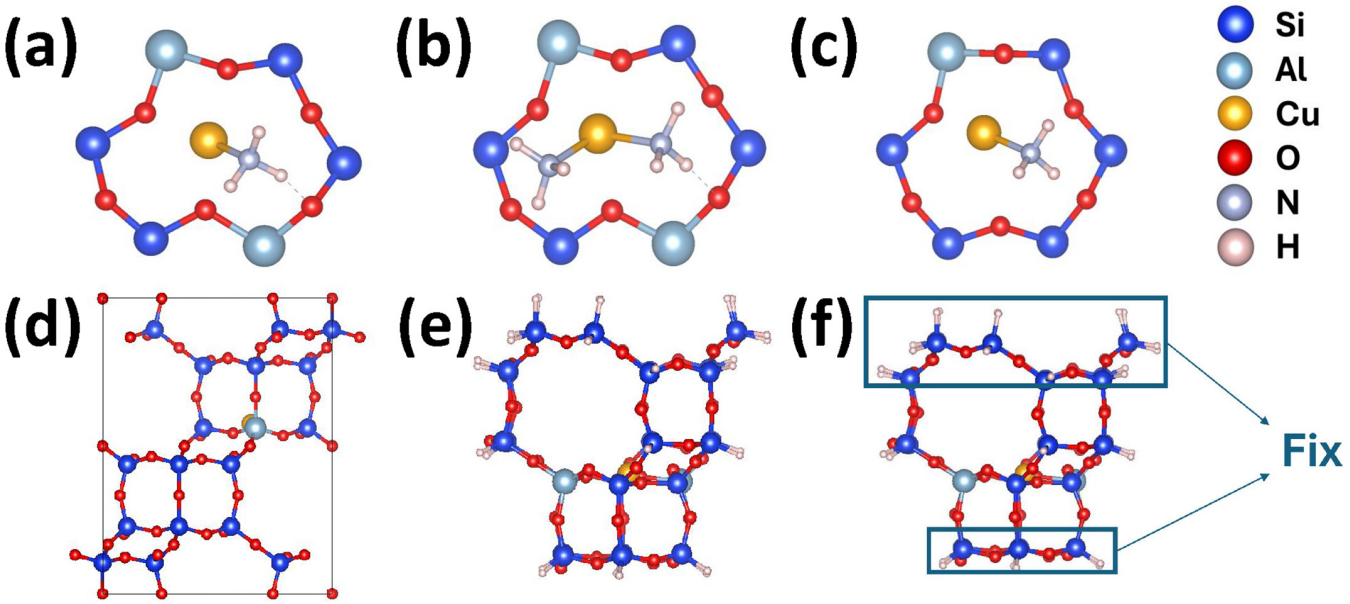


Figure 8. Cu-SSZ-13 zeolite catalyst model: (**a**) Cu-tethered 6-membered ring with 2 Al and 1 adsorbed NH_3 (Z_2-1), (**b**) Cu-tethered 6-membered ring with 2 Al and 2 adsorbed NH_3 (Z_2-2), (**c**) Cu-tethered 6-membered ring with 1 Al and 1 adsorbed NH_3 (Z-1), (**d**) periodic model showing the unit cell, (**e**) cluster model, (**f**) cluster model with fixed atoms.

In the temperature range of 200–550 °C and at an NH_3 concentration of 750 ppm—conditions consistent with a recent experimental study on NH_3-SCR with CH_2O [15]—singly and doubly NH_2-coordinated Cu species have been identified as the most stable [38]. Accordingly, three starting models were considered in this work: Z-1 (corresponding to Cu^{+}), and Z_2-1 and Z_2-2 (corresponding to Cu^{2+}). The model Z-2 (Cu^{+}) was not considered, as it is stable only within a narrow low-temperature range [38].

A commonly used catalyst model for NH_3-SCR on Cu-SSZ-13 zeolites in the literature [6,38,39] is the dynamically solvated and mobile $Cu(NH_3)_2$ moiety. This model is briefly considered in our analysis; however, detailed simulations were not performed due to the very strong binding of reaction intermediates.

4.2. Computational Details

The cluster model described above was used to perform free energy and NEB calculations using ORCA (v5.0.4) [40]. All calculations were carried out using the B3LYP functional [41–44] with the Valence double-zeta basis set (def2-SVP) [45,46] and DFT-D3 dispersion correction [47]. NEB calculations were considered converged when the maximum force was below 10^{-3} Hartree/Bohr and the root-mean-square (RMS) force was below 3×10^{-4} Hartree/Bohr. Single-point free energy calculations were considered converged when the change in energy was less than 10^{-6} Hartree.

For each mechanistic step, the reactant and product structures were first optimized to their minimum-energy configurations. Using these optimized structures as endpoints, nudged elastic band (NEB) calculations were performed to locate the transition states (TS). The NEB-TS approach was employed, wherein the saddle point was first approximated using

the climbing-image NEB (CI-NEB) method and subsequently refined using the Eigenvector Following method [48].

Thermochemical frequency calculations were then carried out to determine the free energies of all states, including reactants, intermediates, products, and transition states. These calculations were performed with all zeolite framework atoms fixed. This approximation is justified by previous literature on zeolite modeling [49], which shows that the entropic and zero-point vibrational energy contributions of distant framework atoms largely cancel when comparing relative reaction barriers; therefore, analyses based on relative TOFs and free energy spans remain reliable without requiring full-cluster Hessians. A temperature of 473 K (200 °C) was used for the entropy contribution to the Gibbs free energy. Although this temperature is relatively low for NH_3-SCR, HCN emissions over Cu-SSZ-13 have been observed experimentally under such conditions [14,15,19]. While some studies report increased HCN emissions at higher temperatures (250–350 °C) [14,19], others show that HCN emissions decrease to nearly zero above 250 °C [15]. These discrepancies may arise from differences in Cu loading and Si/Al ratios resulting from varying synthesis procedures. A standard pressure of 1 atm was used during the free energy calculations.

The final reaction pathways presented in Section 2 connect all identified states and summarize the relevant intermediates (local minima) and transition states (saddle points). The cluster model employed in this work remains relatively large (106 atoms for the Z_2Cu framework, excluding gas-phase or adsorbed species). To address convergence challenges in NEB calculations, free-end NEB and zoom-NEB methods were applied. These approaches improved the resolution of images near the saddle point along the reaction path, facilitating better convergence.

4.3. Kinetics Modelling

To compare reaction rates of different pathways, the turnover frequency (TOF) was calculated (Equation (3)) using the Energetic Span Model [20,21]. In Equation (3), k_B is the Boltzmann constant, h is the Planck's constant, R is the ideal gas constant, T is the temperature, and ΔG_r is the overall free energy change in the reaction cycle. T_i and I_j denote the free energies of transition states and intermediates, respectively. The term $\delta G_{i,j}$ represents the relative free energy between these two states: if T_i appears after I_j, then $\delta G_{i,j} = \Delta G_r$; if T_i appears before I_j, then $\delta G_{i,j} = 0$ (Equation (4)).

$$TOF = \frac{k_B T}{h} \frac{e^{-\frac{\Delta G_r}{k_B T}} - 1}{\sum_{i,j=1}^{N} e^{\frac{T_i - I_j + \delta G_{i,j}}{k_B T}}} \tag{3}$$

$$\delta G_{i,j} = \begin{cases} \Delta G_r & if \quad T_i \; after \; I_j \\ 0 & if \quad T_i \; before \; I_j \end{cases} \tag{4}$$

In most cases, the denominator of Equation (4) is dominated by a single term, which corresponds to the turnover frequency determining intermediate (TDI) and turnover frequency determining transition state (TDTS). Accordingly, Equation (4) can be simplified to Equation (5), where ΔG represents the *energy span* defined by the TDI and TDTS, as given in Equation (6).

$$TOF = \frac{k_B T}{h} e^{-\frac{\Delta G}{k_B T}} \tag{5}$$

$$\Delta G = \begin{cases} G_{TDTS} - G_{TDI} & if \; TDTS \; after \; TDI \\ G_{TDTS} - G_{TDI} + \Delta G_r & if \; TDTS \; before \; TDI \end{cases} \tag{6}$$

While the scalar influence of species concentration on TOFs is important, it is less significant than the energy span, which affects TOFs exponentially [21]. Nevertheless, concentration effects are included in the TOF calculations according to Equation (7). The full expressions are provided in the SI (Equations (S1)–(S3)).

The identification of the TDI and TDTS follows directly from the Energetic Span Model. In the absence of concentration effects, all intermediates and transition states along a given catalytic cycle are considered, and the TDTS–TDI pair is defined as the combination that maximizes the energetic span (ΔG), i.e., the free energy difference between a transition state and a preceding intermediate (accounting for the cyclic nature of the catalytic pathway). This pair determines the rate-limiting segment of the cycle and thus the TOF.

When concentration effects are included, the free energies of intermediates and transition states are adjusted according to the chemical potentials of reactants and products (as described in Equations (6) and (7)) [21]. The TDI and TDTS are then identified as the intermediate–transition state pair that yields the maximum effective free energy span under these conditions. In practice, this involves evaluating all possible TDTS–TDI combinations along the catalytic cycle and selecting the pair that provides the largest contribution to the denominator of the TOF expression.

This procedure is applied consistently to all pathways analyzed in this work (Figures 2–5). Notably, the identified TDI and TDTS do not necessarily correspond to the lowest-energy intermediate or highest-energy transition state, but rather to the states that maximize the (concentration-dependent) energetic span and thus control the overall TOF.

$$TOF = \frac{k_B T}{h} e^{-\frac{\Delta G}{k_B T}} \prod \frac{[R]}{[P]}\Bigg|_{from\ TDI\ to\ TDTS} \quad (7)$$

The species concentration values assumed in this work are listed in Table 4. These values were taken from recently reported experimental measurements on NH_3-SCR with CH_2O [15]. For species that were not detectable, a concentration of 1 ppm was assigned instead of 0 to avoid undefined or infinite TOF values. Water is known to have a significant impact on HCN formation [13]. To assess this effect, two H_2O concentrations were considered: the experimentally measured value of 8% (80,000 ppm), representative of real exhaust aftertreatment conditions [15], and 1 ppm to approximate dry conditions.

Table 4. Species concentration used for TOF calculation.

Species	Concentration
CH_2O	1 ppm
NH_3	500 ppm
H_2O	80,000/1 ppm
NO_2	1 ppm
NO	250 ppm
HCN	25 ppm
CO	35 ppm

5. Conclusions

This work investigated the various reaction pathways of CH_2O in NH_3-SCR over Cu-SSZ-13 zeolite catalyst using an ab initio kinetics approach. The free energies of different CH_2O reaction pathways were further analyzed using the Energetic Span Model to compare their relative TOFs, while accounting for species concentration effects. The results show that HCN formation from CH_2O is catalyzed, with the pathway involving methylene

imine (CH_2NH) being the most favorable under typical reaction conditions. A key role of the Cu sites is to lower the energy barrier for the decomposition of aminomethanol (NH_2CH_2OH) to CH_2NH. These findings are consistent with reports of hexamethylenetetramine (HMT) formation during NH_3-SCR with CH_2O, for which methylene imine is a critical intermediate [33,34].

Cu in +1 oxidation state is found to be a more effective catalyst for HCN formation than Cu in the +2 state. In the presence of NO_2 as an oxidant, CH_2O conversion to CO via formic acid formation is significantly faster than any of the HCN formation pathways, consistent with experimentally observed decreases in HCN emissions at higher NO_2 concentrations. Mechanistically, this behavior is attributed to the rapid reaction between CH_2O and NO_2 over Cu sites.

This work also examines the dependence of HCN versus CO selectivity on H_2O concentration and finds that CO selectivity decreases with decreasing H_2O concentration. From a mechanistic perspective, this trend arises because H_2O plays a catalytic role in HCOOH decomposition. In the absence of H_2O, the preferred HCN formation pathway is predicted to shift, as lower H_2O concentrations facilitate dehydration steps.

While this work explores the effects of NO_2 and H_2O on HCN formation from CH_2O over Cu-SSZ-13, several questions remain to be addressed for a more comprehensive understanding. In particular, the subsequent reactivity of the produced HCN with other components of the gas mixture warrants further investigation. For example, HCN has been reported to react directly with NO_2 over Ba-Y type FAU zeolites [50], but this process has not yet been studied at a fundamental level for Cu-SSZ-13.

Furthermore, recent studies highlight the role of the ZCuOH site—an important intermediate in the NH_3-SCR mechanism—as particularly active for HCN conversion [19]. Another study reports the hydrolysis of HCN over Fe-BEA catalysts [32]. A detailed atomistic investigation of the subsequent reactions of HCN over Cu-SSZ-13 under NH_3-SCR conditions is the focus of our ongoing work.

Supplementary Materials: The following supporting information can be downloaded at: https://www.mdpi.com/article/10.3390/catal16050484/s1, Figure S1: Comparison of the adsorption energy with different calculation methods; Figures S2–S5: Free energy diagram of reaction pathways over Z_2-2; Table S1: Comparison of the adsorption energy between Z_2-2 model with Cu in the 6-membered ring and the solvated mobile Cu; Table S2: Comparison of relative TOFs between Z_2-2 model with Cu in the 6-membered ring and the solvated mobile Cu; Table S3: TDI, TDTS, energy span, important species and relative TOF results of different pathways and active sites, [H_2O] = 1 ppm; Equations (S1)–(S3): TOF calculation with species concentration; Equations (S4)–(S17): Mechanistic details of reaction pathways.

Author Contributions: The manuscript was written through contributions of all authors. S.T. primarily performed the calculations and developed the analysis routines. N.L. contributed by performing part of the DFT calculations and analysis. P.C. and A.K. devised the research plan and supervised the project. A.K. acquired research funding. All authors have read and agreed to the published version of the manuscript.

Funding: The authors gratefully acknowledge funding by the Deutsche Forschungsgemeinschaft (DFG, German Research Foundation) under Germany's Excellence Strategy—Cluster of Excellence 2186/2 "The Integrated Fuel & Chemical Science Center"—ID: 390919832.

Data Availability Statement: Data for this article, including nudged elastic band trajectories, optimized intermediates, and transition states are available at Science Data Bank at https://doi.org/10.57760/sciencedb.32232.

Acknowledgments: The authors gratefully acknowledge the computing time provided to them at the NHR Center NHR4CES at TU Darmstadt (project number p0021065). This is funded by the

Federal Ministry of Research, Technology and Space, and the state governments participating on the basis of the resolutions of the GWK for national high-performance computing at universities (www.nhr-verein.de/unsere-partner (accessed on 1 November 2023)). Part of the computations were also performed with computing resources granted by RWTH Aachen University under project rwth1467.

Conflicts of Interest: The authors declare no conflicts of interest.

Abbreviations

The following abbreviations are used in this manuscript:

NO_x	Nitrogen oxides
TOF	Turnover frequency
HMT	Hexamethylenetetramine
NH_3-SCR	Ammonia-assisted selective catalytic reduction
VWTi	V_2O_5/WO_3-TiO_2
TDI	Turnover frequency determining intermediate
TDTS	Turnover frequency determining transition state
Z-1	Cu^+ site with one Al and one adsorbed NH_3
Z-2	Cu^+ site with one Al and two adsorbed NH_3
Z_2-1	Cu^{2+} site with two Al and one adsorbed NH_3
Z_2-2	Cu^{2+} site with two Al and two adsorbed NH_3

References

1. Lott, P.; Casapu, M.; Grunwaldt, J.-D.; Deutschmann, O. A Review on Exhaust Gas After-Treatment of Lean-Burn Natural Gas Engines—From Fundamentals to Application. *Appl. Catal. B Environ.* **2024**, *340*, 123241. [CrossRef]
2. Elkaee, S.; Phule, A.D.; Yang, J.H. Advancements in (SCR) Technologies for NOx Reduction: A Comprehensive Review of Reducing Agents. *Process Saf. Environ. Prot.* **2024**, *184*, 854–880. [CrossRef]
3. Duan, C.; Zhang, Y.; Han, S.; Shan, Y.; Du, J.; Wang, M.; Shan, W. Recent Advances in Zeolites for the Selective Catalytic Reduction of NOx with NH3. *Catal. Rev.* **2024**, *68*, 422–483. [CrossRef]
4. Ye, B.; Jeong, B.; Lee, M.; Kim, T.H.; Park, S.-S.; Jung, J.; Lee, S.; Kim, H.-D. Recent Trends in Vanadium-Based SCR Catalysts for NOx Reduction in Industrial Applications: Stationary Sources. *Nano Converg.* **2022**, *9*, 51. [CrossRef]
5. Arnarson, L.; Falsig, H.; Rasmussen, S.B.; Lauritsen, J.V.; Moses, P.G. A Complete Reaction Mechanism for Standard and Fast Selective Catalytic Reduction of Nitrogen Oxides on Low Coverage VOx/TiO_2(001) Catalysts. *J. Catal.* **2017**, *346*, 188–197. [CrossRef]
6. Chen, L.; Janssens, T.V.W.; Vennestrøm, P.N.R.; Jansson, J.; Skoglundh, M.; Grönbeck, H. A Complete Multisite Reaction Mechanism for Low-Temperature NH_3-SCR over Cu-CHA. *ACS Catal.* **2020**, *10*, 5646–5656. [CrossRef]
7. Feng, Y.; Janssens, T.V.W.; Vennestrøm, P.N.R.; Jansson, J.; Skoglundh, M.; Grönbeck, H. High-Temperature Reaction Mechanism of NH_3-SCR over Cu-CHA: One or Two Copper Ions? *J. Phys. Chem. C* **2024**, *128*, 6689–6701. [CrossRef]
8. Janssens, T.V.W.; Falsig, H.; Lundegaard, L.F.; Vennestrøm, P.N.R.; Rasmussen, S.B.; Moses, P.G.; Giordanino, F.; Borfecchia, E.; Lomachenko, K.A.; Lamberti, C.; et al. A Consistent Reaction Scheme for the Selective Catalytic Reduction of Nitrogen Oxides with Ammonia. *ACS Catal.* **2015**, *5*, 2832–2845. [CrossRef]
9. Zhang, R.; Liu, N.; Lei, Z.; Chen, B. Selective Transformation of Various Nitrogen-Containing Exhaust Gases toward N_2 over Zeolite Catalysts. *Chem. Rev.* **2016**, *116*, 3658–3721. [CrossRef]
10. Lott, P.; Deutschmann, O. Lean-Burn Natural Gas Engines: Challenges and Concepts for an Efficient Exhaust Gas Aftertreatment System. *Emiss. Control Sci. Technol.* **2021**, *7*, 1–6. [CrossRef]
11. Wei, H.; Zhang, Z.; Zhang, X.; Dong, F.; Yuan, W.; Chen, H. Overview for Methanol and Formaldehyde Unregulated Emissions of Methanol Fueled Engines. *J. Energy Inst.* **2025**, *120*, 102089. [CrossRef]
12. Zubel, M.; Lehrheuer, B.; Pischinger, S. Impact of Increased Injector Nozzle Hole Diameters on Engine Performance, Exhaust Particle Distribution and Methane and Formaldehyde Emissions during Dimethyl Ether Operation. *Int. J. Engine Res.* **2021**, *22*, 503–515. [CrossRef]
13. Elsener, M.; Nuguid, R.J.G.; Kröcher, O.; Ferri, D. HCN Production from Formaldehyde during the Selective Catalytic Reduction of NOx with NH_3 over V_2O_5/WO_3-TiO_2. *Appl. Catal. B Environ.* **2021**, *281*, 119462. [CrossRef]
14. Zengel, D.; Koch, P.; Torkashvand, B.; Grunwaldt, J.; Casapu, M.; Deutschmann, O. Emission of Toxic HCN During NOx Removal by Ammonia SCR in the Exhaust of Lean-Burn Natural Gas Engines. *Angew. Chem. Int. Ed.* **2020**, *59*, 14423–14428. [CrossRef]

15. Alvarez, A.A.S.; Özyalcin, C.; Padeken, T.; Mauermann, P.; Lehrheuer, B.; Sterlepper, S.; Abouserie, A.; Vennewald, M.; Simon, U.; Palkovits, R.; et al. Impact of Unintentionally Formed CH_2O in Oxygenated Fuel Exhausts on DeNOx-SCR at Different NO_2/NOx Ratios under Close to Real Conditions. *Catal. Sci. Technol.* **2023**, *13*, 4069–4081. [CrossRef]
16. Zengel, D.; Barth, S.; Casapu, M.; Grunwaldt, J.-D. The Impact of Pressure and Hydrocarbons on NOx Abatement over Cu- and Fe-Zeolites at Pre-Turbocharger Position. *Catalysts* **2021**, *11*, 336. [CrossRef]
17. Nuguid, R.J.G.; Elsener, M.; Ferri, D.; Kröcher, O. Operando Diffuse Reflectance Infrared Detection of Cyanide Intermediate Species during the Reaction of Formaldehyde with Ammonia over V_2O_5/WO_3-TiO_2. *Appl. Catal. B Environ.* **2021**, *298*, 120629. [CrossRef]
18. Ngo, A.B.; Vuong, T.H.; Atia, H.; Bentrup, U.; Kondratenko, V.A.; Kondratenko, E.V.; Rabeah, J.; Ambruster, U.; Brückner, A. Effect of Formaldehyde in Selective Catalytic Reduction of NOx by Ammonia (NH_3-SCR) on a Commercial V_2O_5-WO_3/TiO_2 Catalyst under Model Conditions. *Environ. Sci. Technol.* **2020**, *54*, 11753–11761. [CrossRef]
19. Barth, S.; Zengel, D.; Goncalves, T.J.; Plessow, P.N.; Studt, F.; Grunwaldt, J.-D.; Casapu, M. Tailoring the Active Sites in Cu-SSZ-13 as a Catalyst for the Selective Catalytic Reduction of NH_3 to Minimize HCHO and HCN Emissions. *Nat. Catal.* **2025**, *8*, 804–821. [CrossRef]
20. Kozuch, S.; Shaik, S. Kinetic-Quantum Chemical Model for Catalytic Cycles: The Haber−Bosch Process and the Effect of Reagent Concentration. *J. Phys. Chem. A* **2008**, *112*, 6032–6041. [CrossRef] [PubMed]
21. Kozuch, S.; Shaik, S. How to Conceptualize Catalytic Cycles? The Energetic Span Model. *Acc. Chem. Res.* **2011**, *44*, 101–110. [CrossRef] [PubMed]
22. Liu, C.; Yasumura, S.; Toyao, T.; Maeno, Z.; Shimizu, K. Mechanism of Standard NH_3–SCR over Cu-CHA via NO^+ and HONO Intermediates. *J. Phys. Chem. C* **2022**, *126*, 11594–11601. [CrossRef]
23. Ali, M.A. Theoretical Study on the Gas Phase Reaction of CH_2O + NH_3: The Formation of CH_2O NH_3, NH_2CH_2OH, or CH_2NH + H_2O. *Phys. Chem. Chem. Phys.* **2019**, *21*, 19242–19251. [CrossRef]
24. Nguyen, V.S.; Orlando, T.M.; Leszczynski, J.; Nguyen, M.T. Theoretical Study of the Decomposition of Formamide in the Presence of Water Molecules. *J. Phys. Chem. A* **2013**, *117*, 2543–2555. [CrossRef]
25. Darla, N.; Sharma, D.; Sitha, S. Formation of Formamide from HCN + H_2O: A Computational Study on the Roles of a Second H2O as a Catalyst, as a Spectator, and as a Reactant. *J. Phys. Chem. A* **2020**, *124*, 165–175. [CrossRef]
26. Pantaleone, S.; Salvini, C.; Zamirri, L.; Signorile, M.; Bonino, F.; Ugliengo, P. A Quantum Mechanical Study of Dehydration vs. Decarbonylation of Formamide Catalysed by Amorphous Silica Surfaces. *Phys. Chem. Chem. Phys.* **2020**, *22*, 8353–8363. [CrossRef]
27. Tokmakov, B.I.V.; Hsu, C.-C.; Lin, L.V.M.A.M.C. Thermal Decomposition of Formic Acid in the Gas Phase: Bimolecular and H2O Catalysed Reactions. *Mol. Phys.* **1997**, *92*, 581–586. [CrossRef]
28. Wang, B.; Hou, H.; Gu, Y. New Mechanism for the Catalyzed Thermal Decomposition of Formic Acid. *J. Phys. Chem. A* **2000**, *104*, 10526–10528. [CrossRef]
29. Janssens, T.V.W.; Borfecchia, E.; Lomachenko, K.A.; Grönbeck, H.; Berlier, G. The $[(NH_3)_4\ Cu_2\ O_2\ ]^{2+}$-Peroxo Complex as the Key Intermediate for NH_3-SCR Activity and Deactivation of Cu-CHA Catalysts. *ChemCatChem* **2024**, *16*, e202400384. [CrossRef]
30. Berry-Gair, J.; Corà, F. Computational Study of the NH_3 De-NOX Selective Catalytic Reduction on the Mono-Cu Active Site of Cu-SSZ-13. Doctoral Dissertation, UCL (University College London), London, UK, 2023.
31. Paolucci, C.; Verma, A.A.; Bates, S.A.; Kispersky, V.F.; Miller, J.T.; Gounder, R.; Delgass, W.N.; Ribeiro, F.H.; Schneider, W.F. Isolation of the Copper Redox Steps in the Standard Selective Catalytic Reduction on Cu-SSZ-13. *Angew. Chem. Int. Ed.* **2014**, *53*, 11828–11833. [CrossRef]
32. Han, L.; Feng, W.; Jin, Q.; Xu, J.; Wu, Z.; Li, J.; Zhu, J.; Wang, W.; Gao, E.; Yao, S.; et al. Catalytic Hydrolysis of HCN on the Coupled Sites of Lewis Acid and Surface Hydroxyl of Fe-BEA Catalyst Leading to the Presence of HCHO Positively Affects NH3-SCR Activity. *Chem. Eng. J.* **2024**, *500*, 156620. [CrossRef]
33. Vinogradoff, V.; Fray, N.; Duvernay, F.; Briani, G.; Danger, G.; Cottin, H.; Theulé, P.; Chiavassa, T. Importance of Thermal Reactivity for Hexamethylenetetramine Formation from Simulated Interstellar Ices. *Astron. Astrophys.* **2013**, *551*, A128. [CrossRef]
34. Vinogradoff, V.; Rimola, A.; Duvernay, F.; Danger, G.; Theulé, P.; Chiavassa, T. The Mechanism of Hexamethylenetetramine (HMT) Formation in the Solid State at Low Temperature. *Phys. Chem. Chem. Phys.* **2012**, *14*, 12309–12320. [CrossRef]
35. Paolucci, C.; Di Iorio, J.R.; Ribeiro, F.H.; Gounder, R.; Schneider, W.F. Catalysis Science of NOx Selective Catalytic Reduction with Ammonia over Cu-SSZ-13 and Cu-SAPO-34. In *Advances in Catalysis*; Elsevier: Amsterdam, The Netherlands, 2016; Volume 59, pp. 1–107.
36. Jónsson, H.; Mills, G.; Jacobsen, K.W. Nudged Elastic Band Method for Finding Minimum Energy Paths of Transitions. In *Proceedings of the Classical and Quantum Dynamics in Condensed Phase Simulations, Villa Marigola, June 1998*; World Scientific: Lerici, Italy, 1998.
37. Goncalves, T.J.; Plessow, P.N.; Studt, F. On the Accuracy of Density Functional Theory in Zeolite Catalysis. *ChemCatChem* **2019**, *11*, 4368–4376. [CrossRef]
38. Paolucci, C.; Di Iorio, J.R.; Schneider, W.F.; Gounder, R. Solvation and Mobilization of Copper Active Sites in Zeolites by Ammonia: Consequences for the Catalytic Reduction of Nitrogen Oxides. *Acc. Chem. Res.* **2020**, *53*, 1881–1892. [CrossRef]

39. Feng, Y.; Creaser, D.; Grönbeck, H. Simplified Kinetic Model for NH_3-SCR over Cu-CHA Based on First-Principles Calculations. *Top. Catal.* **2023**, *66*, 743–749. [CrossRef]
40. Neese, F.; Wennmohs, F.; Becker, U.; Riplinger, C. The ORCA Quantum Chemistry Program Package. *J. Chem. Phys.* **2020**, *152*, 224108. [CrossRef] [PubMed]
41. Becke, A.D. Density-Functional Thermochemistry. III. The Role of Exact Exchange. *J. Chem. Phys.* **1993**, *98*, 5648–5652. [CrossRef]
42. Lee, C.; Yang, W.; Parr, R.G. Development of the Colle-Salvetti Correlation-Energy Formula into a Functional of the Electron Density. *Phys. Rev. B* **1988**, *37*, 785–789. [CrossRef]
43. Vosko, S.H.; Wilk, L.; Nusair, M. Accurate Spin-Dependent Electron Liquid Correlation Energies for Local Spin Density Calculations: A Critical Analysis. *Can. J. Phys.* **1980**, *58*, 1200–1211. [CrossRef]
44. Stephens, P.J.; Devlin, F.J.; Chabalowski, C.F.; Frisch, M.J. Ab Initio Calculation of Vibrational Absorption and Circular Dichroism Spectra Using Density Functional Force Fields. *J. Phys. Chem.* **1994**, *98*, 11623–11627. [CrossRef]
45. Weigend, F.; Ahlrichs, R. Balanced Basis Sets of Split Valence, Triple Zeta Valence and Quadruple Zeta Valence Quality for H to Rn: Design and Assessment of Accuracy. *Phys. Chem. Chem. Phys.* **2005**, *7*, 3297–3305. [CrossRef] [PubMed]
46. Weigend, F. Accurate Coulomb-Fitting Basis Sets for H to Rn. *Phys. Chem. Chem. Phys.* **2006**, *8*, 1057–1065. [CrossRef] [PubMed]
47. Grimme, S.; Antony, J.; Ehrlich, S.; Krieg, H. A Consistent and Accurate Ab Initio Parametrization of Density Functional Dispersion Correction (DFT-D) for the 94 Elements H-Pu. *J. Chem. Phys.* **2010**, *132*, 154104. [CrossRef] [PubMed]
48. Ásgeirsson, V.; Birgisson, B.O.; Bjornsson, R.; Becker, U.; Neese, F.; Riplinger, C.; Jónsson, H. Nudged Elastic Band Method for Molecular Reactions Using Energy-Weighted Springs Combined with Eigenvector Following. *J. Chem. Theory Comput.* **2021**, *17*, 4929–4945. [CrossRef]
49. De Moor, B.A.; Ghysels, A.; Reyniers, M.-F.; Van Speybroeck, V.; Waroquier, M.; Marin, G.B. Normal Mode Analysis in Zeolites: Toward an Efficient Calculation of Adsorption Entropies. *J. Chem. Theory Comput.* **2011**, *7*, 1090–1101. [CrossRef]
50. Szanyi, J.; Kwak, J.H.; Peden, C.H.F. The Catalytic Chemistry of HCN + NO_2 over Na- and Ba-Y,FAU: An in Situ FTIR and TPD/TPR Study. *J. Phys. Chem. B* **2005**, *109*, 1481–1490. [CrossRef]

Disclaimer/Publisher's Note: The statements, opinions and data contained in all publications are solely those of the individual author(s) and contributor(s) and not of MDPI and/or the editor(s). MDPI and/or the editor(s) disclaim responsibility for any injury to people or property resulting from any ideas, methods, instructions or products referred to in the content.